

Approaching the limits of cationic and anionic electrochemical activity with the Li-rich layered rocksalt Li_3IrO_4

Arnaud J. Perez^{1,2,3}, Quentin Jacquet^{1,2,3}, Dmitry Batuk^{1,4}, Antonella Iadecola³, Matthieu Saubanère^{3,5}, Gwenaëlle Rousse^{1,2,3}, Dominique Larcher^{3,6}, Hervé Vezin^{3,7}, Marie-Liesse Doublet^{3,5} and Jean-Marie Tarascon^{1,2,3*}

The Li-rich rocksalt oxides Li_2MO_3 ($M = 3d/4d/5d$ transition metal) are promising positive-electrode materials for Li-ion batteries, displaying capacities exceeding 300 mAh g^{-1} thanks to the participation of the oxygen non-bonding $\text{O}(2p)$ orbitals in the redox process. Understanding the oxygen redox limitations and the role of the O/M ratio is therefore crucial for the rational design of materials with improved electrochemical performances. Here we push oxygen redox to its limits with the discovery of a Li_3IrO_4 compound ($\text{O}/\text{M} = 4$) that can reversibly take up and release 3.5 electrons per Ir and possesses the highest capacity ever reported for any positive insertion electrode. By quantitatively monitoring the oxidation process, we demonstrate the material's instability against O_2 release on removal of all Li. Our results show that the O/M parameter delineates the boundary between the material's maximum capacity and its stability, hence providing valuable insights for further development of high-capacity materials.

Lithium-ion battery technology, widely used in portable electronics, is gaining increasing importance for large-volume applications devoted to electric vehicles and renewable energy sources. This justifies the flourishing research focusing on the improvement of this technology in terms of performance, sustainability and safety. Great hopes are being placed on the design of high-capacity cathode materials relying on the recent discovery of anionic redox activity in layered Li-rich NMC (Ni-Mn-Co)¹. Taking advantage of cumulating both cationic and anionic redox processes within the same compound, materials such as Li-Nb-Mn-O and Li-Mn-O with capacities exceeding 300 mAh g^{-1} were isolated^{2,3}. However, the asset provided by such staggering capacities is negated by capacity fade with cycling, sluggish kinetics of the anionic redox process, and/or surface oxygen depletion in Li-rich NMC. Solving these issues is not only of major importance for practical applications but also essential to push the limits of anionic redox through the design of novel electrode materials optimizing the trade-off between large extra capacity and structural stability.

Such a search is backed-up by theoretical calculations, and the literature is becoming rich in papers aiming at defining guidelines or indicators to conceptually identify materials showing a Li-driven anionic activity⁴⁻⁶. They all agree on the fact that pure oxygen $\text{O}(2p)$ states are required at the Fermi level to reach extra capacities, a situation that can be triggered from the O/M stoichiometry (Fig. 1a). However, the role of the M-O covalence and Li/M cationic disorder on the promotion of these $\text{O}(2p)$ non-bonding orbitals at the Fermi level is still under debate. By experimentally adjusting these parameters, we identified that Li-rich phases, based on $4d$ (Li_2RuO_3) or $5d$ (Li_2IrO_3) metals (that is, with high M-O bond covalence), are

more prone to a reversible anionic redox process and more stable against surface oxygen release than $3d$ -based Li-rich NMC phases^{7,8}. By exploring various polymorphs of the Li_2MO_3 series, we demonstrated that the anionic process is not solely linked to Li-rich phases having a layered ($\text{Li}_{1.2}\text{Ni}_{0.13}\text{Mn}_{0.54}\text{Co}_{0.13}\text{O}_2$)¹ or a disordered rocksalt structure ($\text{Li}_{1.3}\text{Nb}_{0.3}\text{M}_{0.4}\text{O}_2$ with $M = \text{Mn, Fe}$)², but also occurs in fully ordered three-dimensional structures such as $\beta\text{-Li}_2\text{IrO}_3$ (ref. 9). In attempts to achieve electrodes with higher capacities, researchers have explored, beyond LiMO_2 and Li_2MO_3 phases, the $\text{Li}_3\text{NbO}_4\text{-LiMO}_2$ and $\text{Li}_4\text{MoO}_5\text{-NiO}$ solid solutions, with good capacity and cycling at 55°C for $\text{Li}_{1.2}\text{Nb}_{0.4}\text{Mn}_{0.4}\text{O}_2$. However, no electrochemical activity was reported for compounds with a Li/M and O/M ratio higher than 2 and 3 respectively, in particular for Li_3NbO_4 and Li_4MoO_5 (refs 2,10), which are electronic insulators free of d electrons (Nb^{5+} , Mo^{6+}).

To probe the effect of increasing the O/M ratio to reach higher anionic extra capacities, we searched for Li_3MO_4 compounds relying on the transition metal M having a partially filled d -band. In this work, we explored the Li-Ir-O ternary phase diagram and discovered, besides the two α and β Li_2IrO_3 polymorphs, a Li-rich Li_3IrO_4 phase crystallizing in a layered rocksalt structure. Using complementary in situ X-ray diffraction (XRD) and X-ray absorption spectroscopy (XAS) experiments coupled with ex situ electron paramagnetic resonance (EPR), pressure measurements and density functional theory (DFT) calculations, we show that this phase can be either oxidized ($\text{Li}_3\text{IrO}_4 \rightarrow \text{IrO}_4$) or reduced ($\text{Li}_3\text{IrO}_4 \rightarrow \text{Li}_3\text{IrO}_4$), with this amphoteric character being nested in redox processes involving anions on oxidation ($x < 3$ in Li_xIrO_4) and cations on reduction ($x > 3$).

¹Collège de France, Chimie du Solide et Energie, UMR 8260, 11 place Marcelin Berthelot, 75005 Paris, France. ²Sorbonne Universités - UPMC Univ. Paris 06, 4 Place Jussieu, 75005 Paris, France. ³Réseau sur le Stockage Electrochimique de l'Energie (RS2E), FR CNRS 3459, Amiens, France. ⁴EMAT, University of Antwerp, Groenenborgerlaan 171, 2020 Antwerp, Belgium. ⁵Institut Charles Gerhardt, CNRS UMR 5253, Université Montpellier, Place E. Bataillon, 34095 Montpellier, France. ⁶Laboratoire de Réactivité et Chimie des Solides, UMR CNRS 7314, 33 Rue Saint Leu, 80039 Amiens, France. ⁷Université Lille 1, CNRS UMR 8516-LASIR, 59655 Villeneuve d'Ascq, France. *e-mail: jean-marie.tarascon@college-de-france.fr

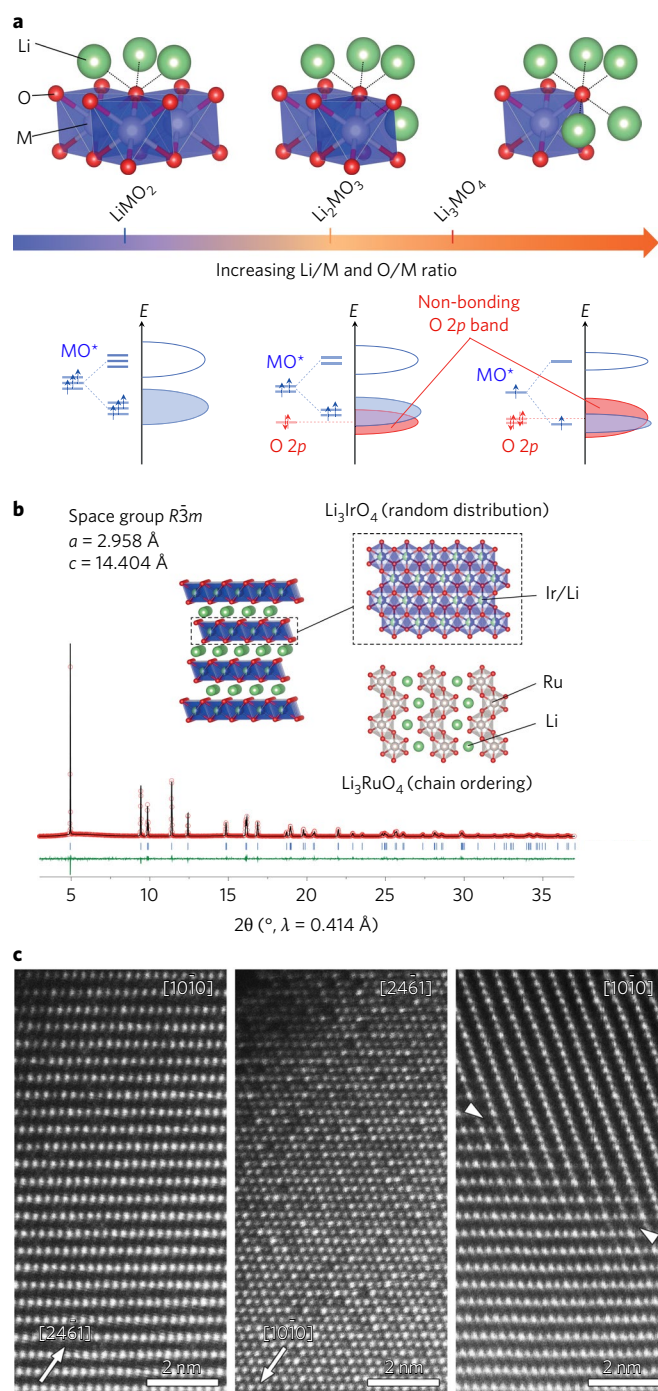


Fig. 1 | Increasing the O/M ratio from Li_2MO_3 to Li_3MO_4 in rocksalt oxides as a strategy to activate anionic redox. **a**, The local structure around oxygen is shown as a function of the O/M or Li/M ratio, with a schematic of the corresponding electronic structure describing the increase of non-bonding O(2p) orbitals at the Fermi level at the expense of antibonding MO^* states. **b**, Rietveld refinement of synchrotron X-ray diffraction for Li_3IrO_4 suggests a layered structure with no long-range ordering of Li and Ir in the metallic layers in contrast to the chain ordering of Li_3RuO_4 . **c**, Typical HAADF-STEM images of Li_3IrO_4 acquired along the $\langle 110 \rangle_{\text{NaCl}}$ directions of the rocksalt sublattice. The indices of the directions are given with respect to the hexagonal $R\bar{3}m$ lattice. The images on the left and in the middle confirm the layered organization of the structure with random cation distribution in the Li/Ir layers. The image on the right demonstrates coherent intergrowth of structure domains with different orientations (marked with arrowheads).

Rich electrochemical properties

The synchrotron XRD pattern of Li_3IrO_4 (equivalently written as $\text{Li}(\text{Li}_{1/2}\text{Ir}_{1/2})\text{O}_2$) was successfully refined by the Rietveld method using the hexagonal $R\bar{3}m$ description of layered LiMO_2 phases (Fig. 1b and Supplementary Table 1). Among the Li_3MO_4 family, this compound adopts a specific layered rocksalt structure with oxygen atoms in a cubic close-packed arrangement, and Li/Ir occupying all octahedral sites (O3 structure). The cations are organized into pure Li layers alternating with mixed Ir/Li layers, in which Ir and Li are randomly distributed, an arrangement also confirmed by high-angle annular dark-field scanning transmission electron microscopy (HAADF-STEM) imaging (Fig. 1c).

The electrochemical performances of Li_3IrO_4 were tested versus Li in Swagelok cells. Starting on oxidation, the delithiation occurs through a voltage plateau at an average potential of 3.9–4.0 V versus Li^+/Li (Fig. 2a). Strikingly, all Li^+ can be removed from Li_3IrO_4 . Bearing in mind that, in both polymorphs of the parent material Li_2IrO_3 , the electrochemical oxidation of Ir is limited to Ir^{5+} (refs 8,9), this suggests a high level of participation of oxygen in the redox activity. On the subsequent discharge, the voltage profile becomes sloping, with almost 3 Li^+ reinserted down to a lower cutoff of 2.0 V, and remains as such on the next charge/discharge cycles with a fair reversibility. By lowering the voltage down to 0 V, we observe a continuous voltage decrease until 0.7 V, corresponding to the conversion reaction $\text{Li}_x\text{IrO}_y + (2y-x)\text{Li}^+ + (2y-x)e^- \rightarrow \text{Ir} + y\text{Li}_2\text{O}$ (Supplementary Fig. 1), and electrolyte decomposition¹¹. Owing to the presence of Ir^{5+} in the pristine material, we also tested our electrode on reduction and found that Li_3IrO_4 can reversibly intercalate up to 1.7 extra Li (Fig. 2a). This occurs through two well-defined and reversible processes located at 1.9 V and 1.8 V (Supplementary Fig. 2) that are indicative of classical insertion/deinsertion mechanisms involving the $\text{Ir}^{5+}/\text{Ir}^{4+}/\text{Ir}^{3+}$ reduction cascade. While the redox activity of Li_3IrO_4 spans over almost five electrons, it seems impossible to take advantage of the whole capacity due to partial irreversibility of the oxidation process. Overall, the cell shows a reversible capacity of nearly 3.5 electrons per transition metal with a good cyclability over the 25 first cycles (Supplementary Fig. 3) when changing the cycling conditions and limiting the first delithiation to LiIrO_4 (Fig. 2b). This reversible exchange of 3.5 Li^+/M stands as a record among the transition metal oxides reported so far as insertion cathode materials. The rich electrochemistry of Li_3IrO_4 therefore represents an excellent opportunity to investigate in depth the concomitant cationic/anionic redox processes and underpin, via an arsenal of characterization techniques, the science beyond them.

Structural evolution

The lithiation–delithiation mechanism in Li_3IrO_4 was examined by in situ XRD. During cell discharge (Fig. 2c), a continuous increase of all cell parameters (Supplementary Fig. 4) indicates a solid-solution mechanism until $\text{Li}_{3.5}\text{IrO}_4$, together with an increase of the unit-cell volume ($\Delta V/V = +4.2\%$). For x between 3.5 and 4 in Li_xIrO_4 , the intensity of the peaks decreases at the expense of a new phase that becomes pure at $x = 4$. Finally, the Bragg peaks shift continuously up to $x = 4.7$, with the exception of the (00l) peaks, showing that the interlayer distance is preserved. The structure of the fully reduced $\text{Li}_{4.7}\text{IrO}_4$ phase was deduced from XRD and neutron diffraction (Fig. 2f,g) using the structural model of Li_2NiO_2 (ref. 12) (Supplementary Table 2) with the extra Li lying in tetrahedral sites (T1 structure, Fig. 2h). On charging the cell, the solid-solution process is reversed with a shift of all peaks except (00l) to higher angles, and is followed by a biphasic process leading to the original O3 structure. Overall, the structural transition is reversible, but proceeds via different paths on reduction and oxidation, a feature shared by other insertion compounds¹³.

In situ XRD diffraction patterns were similarly collected on a $\text{Li}_3\text{IrO}_4/\text{Li}$ cell started on oxidation (Fig. 2d). We initially observe a

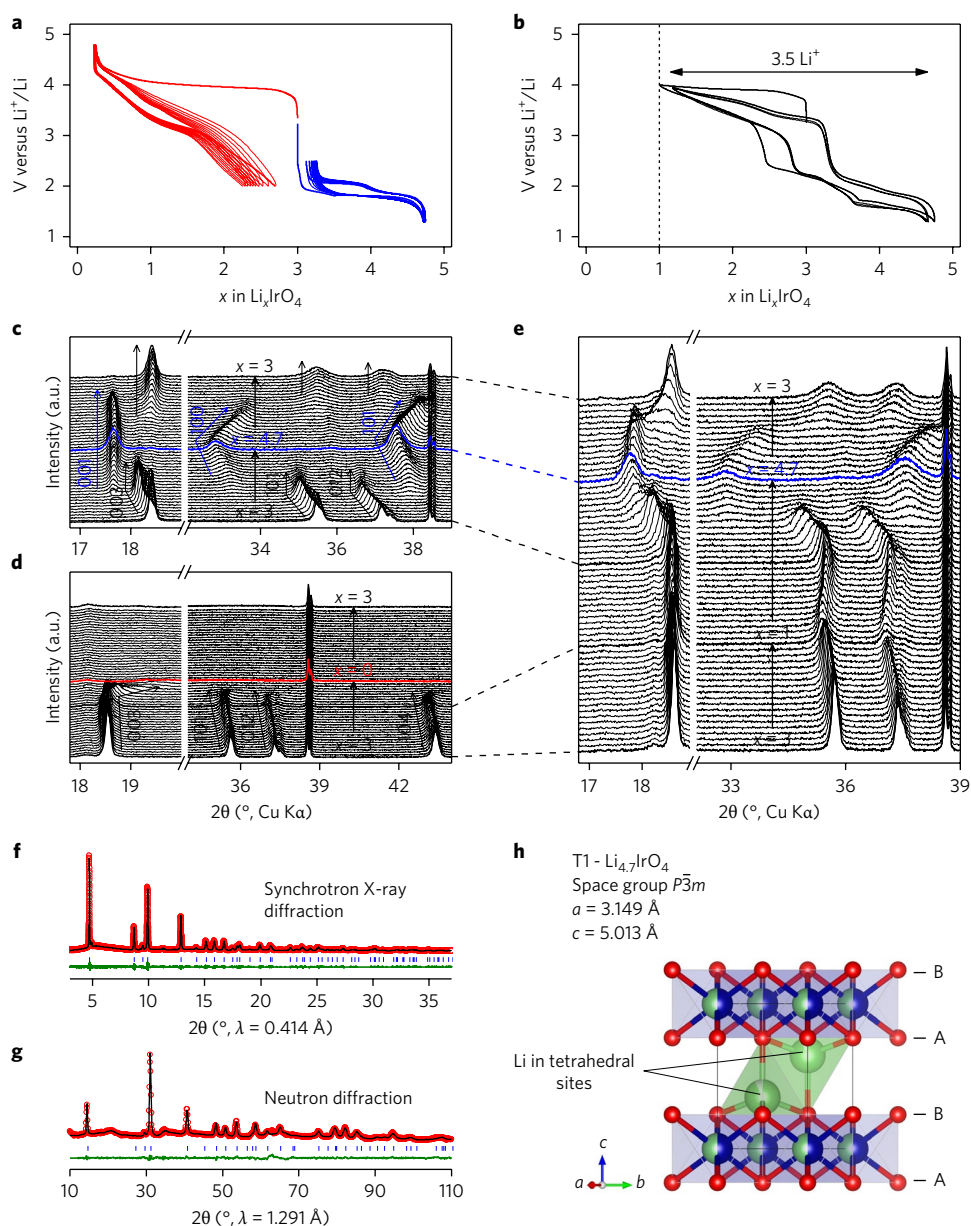


Fig. 2 | Structural evolution of Li_3IrO_4 on electrochemical insertion/deinsertion of Li. **a**, Galvanostatic curves started on oxidation (red) and reduction (blue). **b**, A reversible capacity of 3.5 electrons (340 mAh g^{-1}) can be achieved if the delithiation on the first cycle is stopped at $x=1$. **c**, In situ XRD during the low-voltage process shows a reversible intercalation/deintercalation mechanism, with the formation of a new phase at $x=4.7$. Black labels refer to the O3 structure and blue ones to the T1 structure. **d**, The same experiment on oxidation reveals an irreversible amorphization of the material, explaining the modification of the voltage curve after the first charge. **e**, By stopping the charge at $x=1$, in situ XRD shows that the structure of the material is preserved, as well as the reversible structural transition observed on reduction to 1.3 V. **f-h**, Rietveld refinement of synchrotron X-ray (**f**) and neutron (**g**) diffraction of the fully reduced phase reveals that $\text{Li}_{4.7}\text{IrO}_4$ adopts a T1 stacking similar to Li_2NiO_2 that allows the insertion of extra Li in tetrahedral sites (**h**).

slight shift of all Bragg reflections towards lower angles during delithiation up to $x=1$ in Li_xIrO_4 (Supplementary Fig. 4), followed by a sudden shift towards larger angles and a drastic loss of peak intensity. After three Li^+ are removed, the X-ray powder pattern of fully delithiated ' IrO_4 ' is featureless, indicative of its amorphous nature. This was further confirmed by the electron diffraction pattern of ' IrO_4 ', which shows the survival of only short-range interatomic correlations (Supplementary Fig. 5). Altogether, this explains the observed irreversible capacity of Li_3IrO_4 when delithiated below $x=1$. In contrast, when the cell charge is limited to $x=1$ (Fig. 2e), all Bragg peaks shift back to their initial positions via the $\text{O3} \rightarrow \text{T1}$ transformation, thus unambiguously proving the reversibility of the insertion process over 3.5 electrons.

In light of previous studies, oxygen loss may occur on charge in these high-capacity electrodes. To check this point, gas pressure analysis was carried out over the first two charge/discharge cycles. As Li_xIrO_4 is charged, the pressure stays constant before $x=1$ prior to rapidly increasing for $x < 1$ (Fig. 3a) and remains stable upon further cycling. From the pressure increase and differential electrochemical mass spectrometry (DEMS) analysis (Fig. 3b), we can deduce that approximately 0.35 gas molecules are released per Li_3IrO_4 with the nature of the gas being mainly O_2 ($m/z=32$) with minor amounts of CO_2 ($m/z=44$) at the very end of oxidation. As expected for a four-electron O^{2-}/O_2 transformation, this would lead to an irreversible loss of 1.4 electrons, hence a stoichiometry for the charged product closer to IrO_3 than IrO_4 . Obviously, caution has to

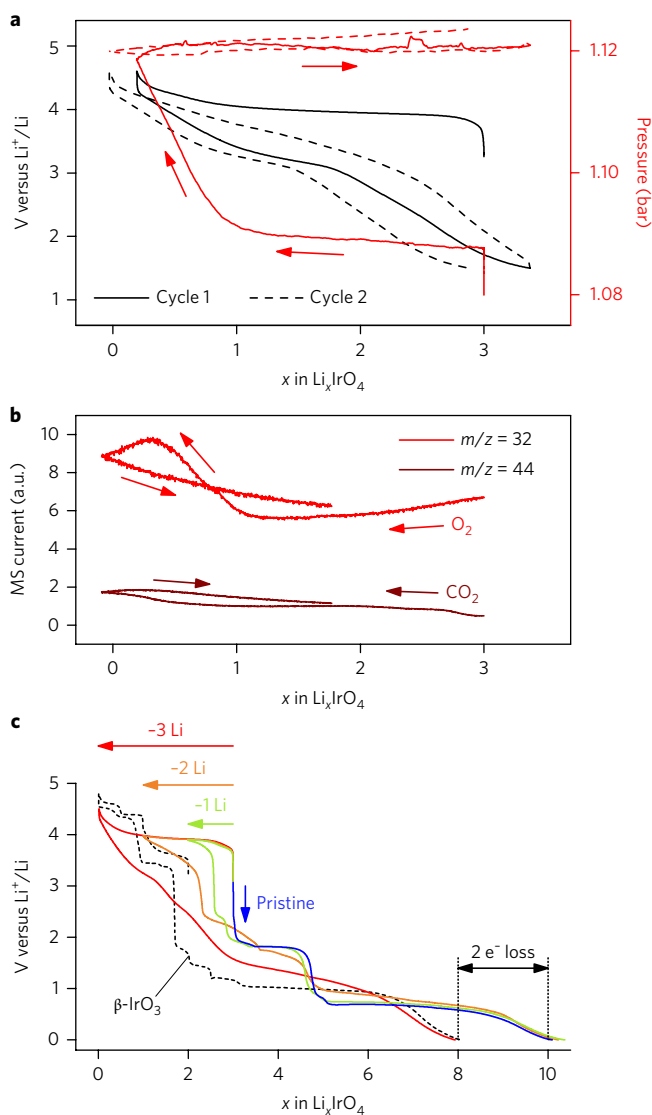


Fig. 3 | Irreversible capacity loss for total delithiation of Li_3IrO_4 . **a**, In situ pressure measurement during the first two cycles of Li_3IrO_4 delithiation. The pressure initially remains constant on oxidation (red curve), but drastically increases as soon as the last Li is removed from the structure. No change is observed afterwards on the next cycle (dashed line). **b**, DEMS analysis of the gas formed shows an increased signal of O_2 in the cell, as well as CO_2 to a lesser extent, suggesting that the material loses oxygen below $x=1$. **c**, Reduction curves for different depths of delithiation. The capacity after complete conversion of the material to Ir^0 and Li_2O does not change for the pristine (blue) or after removing one or two Li^+ (green and orange), but two electrons are lost on reduction when the three Li^+ are removed from the structure (red). The reduction capacity of the amorphous phase after losing gas is similar to that of $\beta\text{-IrO}_3$ (dashed line).

be exercised as this approximation does not take into account the CO_2 component.

Another indirect way to measure the oxygen loss for this highly oxidized sample consists of further exploiting the discharge-driven conversion reaction down to 0 V, with the number of Li taken up (u) in Li_xIrO_y being related to the amount of oxygen y by $u=2y-x$. This assumes similar 0 V end products; that is, Ir nanoparticles embedded into an amorphous Li-based matrix, as confirmed by HAADF-STEM (Supplementary Fig. 6). The discharge capacities of the pristine, partially charged and fully charged Li_xIrO_y materials ($x=3, 2, 1$ and 0)

are shown in Fig. 3c. No difference can be observed between the pristine, $x=1$ and $x=2$ samples, implying that no oxygen is released on oxidation. In contrast, the capacity of the fully charged sample is two electrons lower than that of the pristine material, implying that, on oxidation, amorphization of the material proceeds with the release of one oxygen atom per formula unit. The IrO_3 stoichiometry is further confirmed by the similar discharge capacity measured for the crystalline $\beta\text{-IrO}_3$ obtained by delithiating $\beta\text{-Li}_2\text{IrO}_3$ (Fig. 3c; ref. 9). This material, designated herein as a- IrO_3 (for ‘amorphous IrO_3 ’), is shown to be less stable by 57 kJ mol^{-1} (Supplementary Fig. 7) than its $\beta\text{-IrO}_3$ polymorph. Lastly, the lower number of oxygens released obtained by gas measurement (0.35 O_2) as compared with 0.5 O_2 from electrochemistry is most likely due to partial reactivity of O_2 with the electrolyte and/or carbon SP.

Operando XAS at the Ir L_{III} edge was then carried out on three cells (Fig. 4a): one for the reduction process (cell A), one undergoing full oxidation (cell B) and the last one to test the reversible 3.5 electron cycle after activation to $x=1$ (cell C). All of the data obtained from cell A can be fully described by three individual spectra in various relative proportions during cycling (Fig. 4b), each of them corresponding to well-defined Ir local environments that were characterized by fitting the extended X-ray absorption fine-structure (EXAFS) oscillations (Supplementary Table 3 and Supplementary Fig. 8). We could then deduce the distortion of the IrO_6 octahedra during the Li insertion process by monitoring the Ir–O and Ir–Ir distances (Fig. 4c): both distances increase from the pristine (A1) to the intermediate (A2) and the reduced (A3) components, in agreement with the expected reduction of Ir^{5+} to Ir^{4+} and Ir^{3+} .

For the cell started on oxidation (cell B), five components are needed (Fig. 4b, centre) to satisfactorily describe the data because of the irreversibility of the oxidation process. EXAFS analysis for B1 (pristine) and B2 (intermediate on charge) is very straightforward since the same structural model as for components A1 can be used (Supplementary Table 3). For the B3 (fully charged), B4 (intermediate on discharge) and B5 (discharged) components, new models accounting for the loss of oxygen and the amorphous nature of a- IrO_3 were necessary for satisfactory fits. They show the presence of IrO_6 octahedra having a connectivity increasing from 2 to 3 (Supplementary Fig. 9) as expected from the stoichiometry of a- IrO_3 . Interestingly, the comparison between B1 and B2 components highlights a slight decrease of the Ir–O distances together with an increase of the Ir–Ir distances (Fig. 4c). This implies that Ir is not oxidized but adopts a more distorted IrO_6 environment. The average Ir–O distance eventually increases up to 2.06 \AA for B5, consistent with a significant reduction of Ir on discharge.

Lastly, three components were satisfactorily used both on charge and discharge to describe the cycling of cell C, indicating the reversibility of the process. The most oxidized component (C1) is relatively close to the pristine spectra of the other cells (A1 and B1), whereas the intermediate (C2) and reduced (C3) components show an increase of both the Ir–O and Ir–Ir distances consistent with the reduction of Ir.

Cationic/anionic redox

The operando XANES data were used to get information on the oxidation state of Ir during cycling via monitoring of the intense white line (WL) overlapping with the Ir L_{III} edge (Fig. 5a). The WL probes dipole-allowed $2p\text{-}5d$ transitions and their intensity is proportional to the number of unoccupied d -states for $5d$ metals, as previously reported¹⁴. Thus, the WL intensity (Fig. 5b) is a better parameter to follow the oxidation or reduction of Ir, compared with the energy of the WL (Fig. 5c), which is more sensitive to local distortion of the IrO_6 octahedra. On reduction (cell A, blue), both WL energy and intensity decrease linearly with composition ($\sim 0.84\text{ eV}$ per electron and $\sim 15\%$ per electron respectively) and vice versa on the following oxidation, with both curves having similar slopes, indicative of a reversible process. More quantitatively, the WL intensity

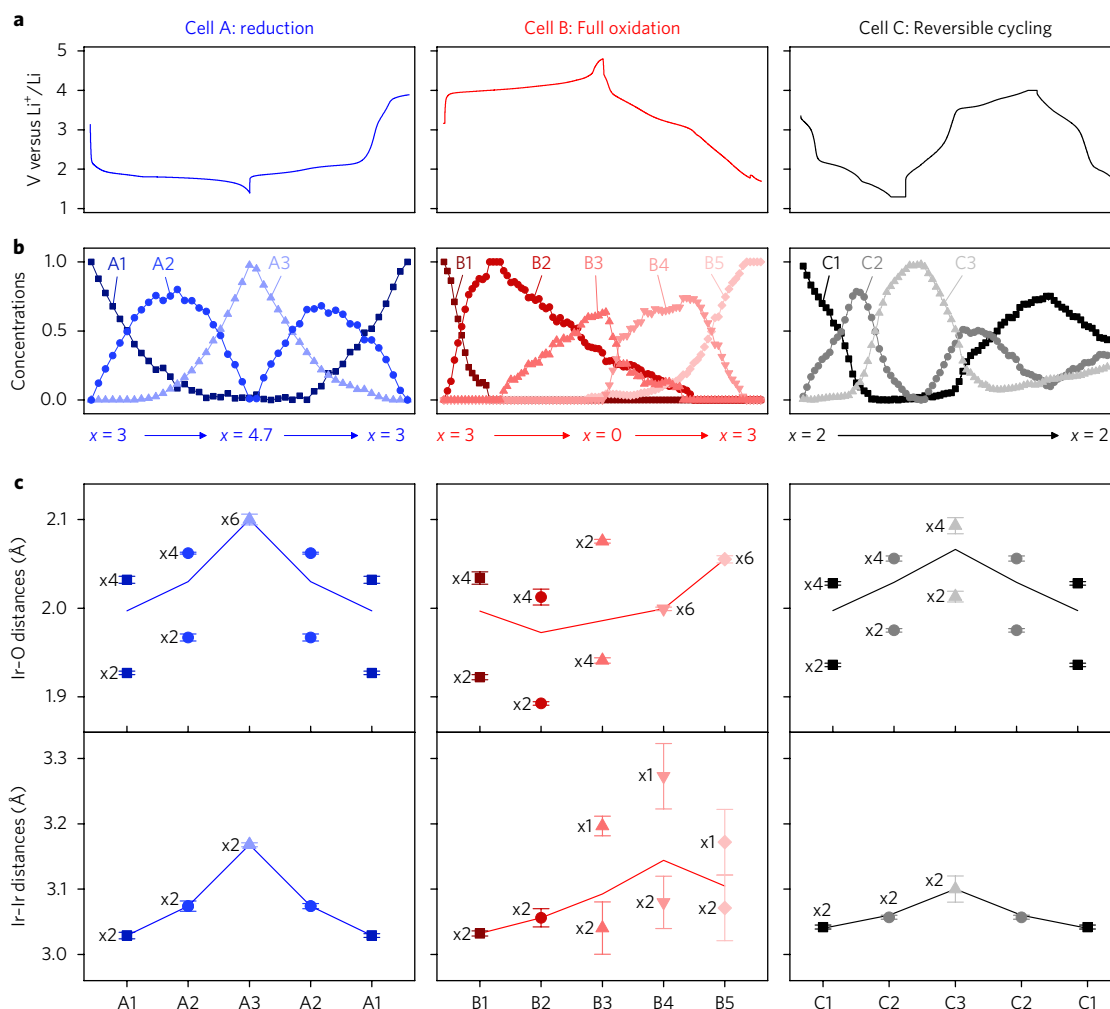


Fig. 4 | Local structural evolution from operando EXAFS analysis at the Ir L_{III} edge. **a**, Quick-XAS measurements were acquired operando with three electrochemical cells cycled in different conditions. Cell A was started on reduction and cycled between $x=3$ and $x=4.7$ in Li_xIrO_4 (left), cell B was fully oxidized to trigger the amorphization before discharging to $x=3$ (centre) and cell C was charged to $x=1$ and partially discharged to $x=2$ before the measurement of a full reversible cycle (right). **b**, Relative concentrations during cycling of the principal components extracted using principal component analysis and multivariate curve resolution-alternating least-squares analysis, showing reversible processes for cell A and C (similar components are used to describe charge and discharge) and an irreversible one for cell B that requires five different components to account for the charge/discharge cycle. Each component is described by a specific marker and colour as depicted in the figure. **c**, Ir-O and Ir-Ir distances obtained from fitting the EXAFS oscillations (Supplementary Figs. 8–10). The multiplicity of each distance is indicated next to the corresponding data point ($\times 1$, $\times 2$, $\times 4$ and $\times 6$, as reported in Supplementary Table 3). Full lines are connecting the average Ir-O and Ir-Ir distances to highlight the distortion of IrO_6 octahedra associated with Ir oxidation/reduction. The error bars were estimated from the distribution of values found for the different models tried during the fitting process.

varies by approximately 24%, which is in good agreement with the 25% decrease in hole population expected from a classical cationic process from Ir^{5+} (d^4) to $\text{Ir}^{3.5+}$ ($d^{5.5}$) and predicted from DFT Bader charge analyses (Supplementary Fig. 11).

On oxidation (cell B, red) both the position in energy (Fig. 5c) and the intensity (Fig. 5b) of WL slightly increase, prior to stabilizing and slowly decreasing once ~ 0.5 Li^+ is removed. This suggests that oxygen is primarily oxidized instead of iridium during the charging process, although the shift observed at the very early stage of charge cannot discard a hint of Ir^{6+} . Indeed, while such a high oxidation state has never been achieved in the Ir-based rocksalt oxides reported so far^{8,9}, it has already been stabilized in more ionic perovskites^{15,16}. To address this question, electronic-structure DFT calculations, including full structural relaxations were performed at $x=3$, 2 and 1 (Supplementary Table 4 and Supplementary Fig. 11). The results show a major contribution of the oxygen states below the Fermi level in the electronic structure of Li_3IrO_4 that confirms

the dominant oxygen participation in the redox process below $x=3$, and a limited oxidation of Ir^{5+} accompanied by significant IrO_6 local distortions below $x=3$ that may explain the WL shift in energy. On subsequent discharge, a nonlinear decrease of both WL position and area is observed, indicating that both iridium and oxygen participate in the reduction process but their effects cannot be easily disentangled.

During the reversible cycling (cell C, black), both the WL intensity and its position in energy show a non-monotonous evolution, suggesting a larger participation of Ir and O in the lower and higher voltage region, respectively. The extent of Ir oxidation/reduction is definitely lower than for cell A, in agreement with the EXAFS analysis.

EPR measurements were then carried out to probe unpaired spins regardless of whether they belong to cationic or anionic species. Ex situ samples were measured for different states of charge/discharge (Fig. 6a). As expected, the pristine material, which contains

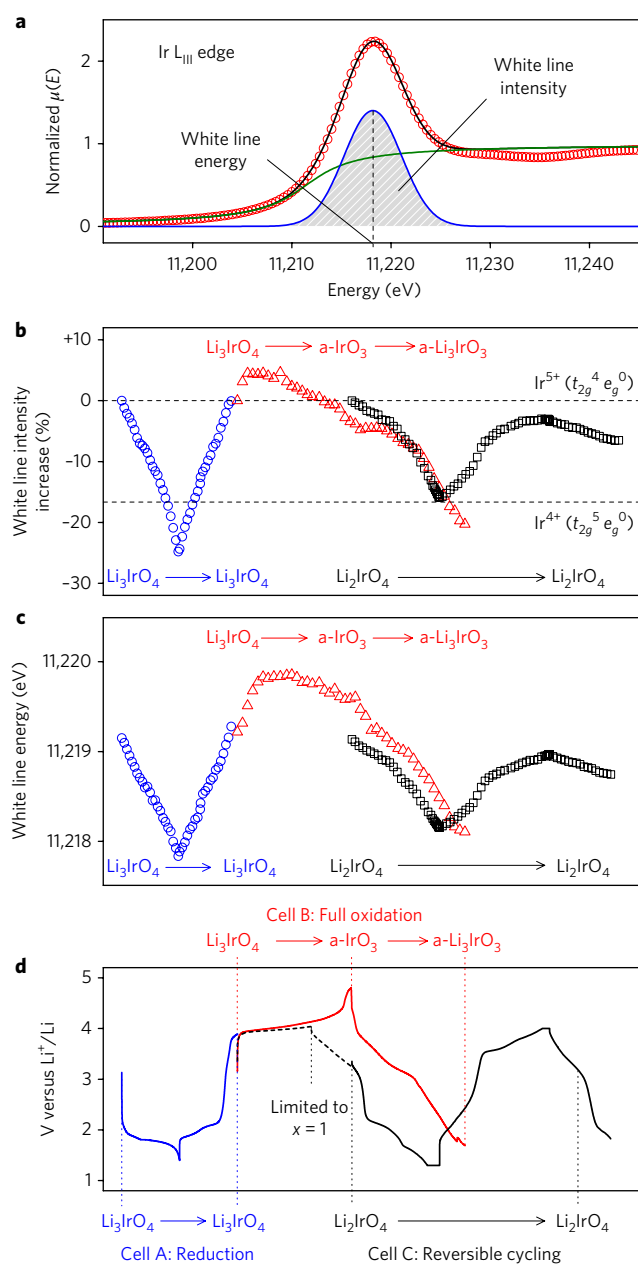


Fig. 5 | Participation of cationic and anionic redox processes during cycling studied by operando XANES. The XANES data were obtained from the same cells described in Fig. 4. **a**, Fitting of the Ir L_{III} edge using an arctangent function for the jump (green) and a Gaussian peak for the white line (WL; blue). Experimental points and the result of the fit are represented by red circles and a black curve, respectively. **b**, Changes in WL intensity during cycling for the three cells: A (blue circles), B (red triangles) and C (black squares). The WL corresponds to the 2*p*-5*d* electronic transition and its intensity varies depending on the 5*d* hole population. The dashed lines highlight the change from Ir⁵⁺ to Ir⁴⁺. **c,d**, Changes in energy of the WL are also reported for comparison (**c**) and the corresponding voltage curves for each cell (**d**). The dashed portion in the cycling curve of cell C represents the charge/discharge process performed prior to the measurement. The three data sets were shifted horizontally in the plot to aid comparison, and key compositions are indicated next to the data.

Ir⁵⁺ (EPR-silent) and O²⁻ (diamagnetic), gives no signal (Fig. 6b, (i)). In contrast, the EPR spectrum of the fully reduced sample (Li_{4.7}IrO₄) shows a broad and anisotropic signal (ii) associated with Ir⁴⁺, which

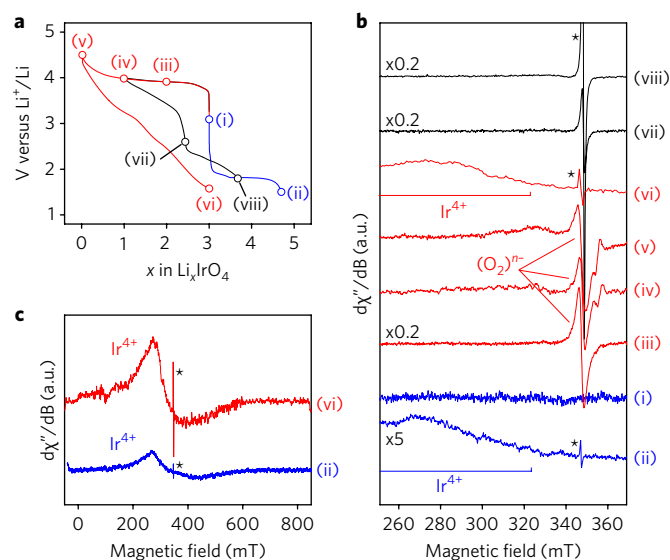


Fig. 6 | Ex situ EPR spectroscopy study of paramagnetic species at different states of charge. **a**, Ex situ samples were measured after cycling in different conditions. **b**, The EPR spectra of the different samples. It should be recalled here that Ir⁵⁺ (*d*⁴), Ir³⁺ (*d*⁶) and (O₂)²⁻ are EPR-silent species at the X band in contrast to Ir⁴⁺ (*d*⁵), Ir⁶⁺ (*d*³) or (O₂)³⁻ and (O₂)⁻ species. The signatures of Ir⁴⁺ and (O₂)ⁿ⁻ species are indicated on the figure and the sharp signal of carbon SP is marked by an asterisk. Some spectra were resized for clarity with the scaling factors specified near the corresponding spectrum. **c**, Full-scale view of the spectra containing the large Ir⁴⁺ signal.

can be nicely visualized by plotting the data over the full (0 to 800 mT) scale (Fig. 6c). From integration of the EPR signal, we could calculate a density of about 0.2 spin per Ir. This would correspond to 20% Ir⁴⁺ and 80% EPR-silent Ir, most likely Ir³⁺, a ratio close to that expected from the electrochemical composition Li_{4.7}IrO₄.

On oxidation, following removal of 1 Li⁺ (*x*=2), an intense isotropic signal appears that can be attributed to oxidized (O₂)³⁻ species (iii). This signal becomes approximately five times less intense and more anisotropic (axial symmetry with *g*_{||}=2.012 and *g*_⊥=2.006) on removal of 2 Li⁺ (iv), suggesting an increasing proportion of more oxidized EPR-silent (O₂)²⁻ peroxy species that are known to be highly unstable^{4,5} and may recombine into O₂ gas. This explains why the EPR spectrum remains alike for a-IrO₃ (v) as oxygen is released. The EPR spectra for the cycled ‘a-Li₃IrO₃’ (vi) shows an intense Ir⁴⁺ signal, with an integrated spin density around 0.5 spin per Ir, corresponding to 50% Ir⁴⁺ and 50% EPR-silent Ir. Lastly, for the samples charged to *x*=1 and then discharged to 2.6 and 1.8 V, the disappearance of the isotropic (O₂)ⁿ⁻ signal (vii) at the expense of a sharp signal characteristic of the carbon¹⁷ (viii) indicates the full reduction of peroxy-like species, as expected.

Discussion

In this work, we report the design and synthesis of a Li₃IrO₄ phase, having more oxygen non-bonding states compared with Li₂MO₃ structures and a lower weight per Li of about 30% due to a higher O/M ratio. This phase reversibly takes up 3.5 Li⁺ per transition metal, hence improving on the record of 2.5 Li⁺ previously established for β-Li₃IrO₃ (ref. 9). This unusually high capacity for insertion cathode materials in Li-ion batteries gives an opportunity to address important questions about anionic redox, including the possibility to increase the capacity of materials undergoing cationic and anionic redox, the limit of stability versus degassing and/or phase transition, and the strategies to be implemented in the search for new high-capacity Li-rich cathode materials.

The findings of this work were driven by challenging theoretical predictions that we experimentally verified. Having identified the oxygen lone-pairs in non-bonding $O(2p)$ orbitals as the origin of the anionic redox process, the authors of ref. 4 speculated that greater capacities could be achieved by increasing the number of such labile electrons through a larger O/M ratio in Li-rich rocksalt structures. Bearing in mind that the interaction of $Li(1s)$ with $O(2p)$ orbitals is limited to electrostatic stabilization (that is, no formation of a covalent bond), the interest in compounds with the Li_xMO_4 formula became obvious. Such a direction comes with the risk of increasing the instability of these materials against oxygen recombination/release, hence requiring a careful selection of the transition metal. In that respect, dealing with the network stability of layered rocksalt versus O_2 release, a theoretical paper⁵ was instructive in stating that M–O covalency is required to stabilize the oxygen network, and showing that delithiated rocksalt compounds with $3d$ metals are fully unstable once Li is removed⁵. It was therefore necessary to further increase the $M(d)$ –O covalency by exploring the Li_3IrO_4 phase that falls in the limit of structural stability.

The Li_3IrO_4 compound pushes the anionic redox to its limit with three Li extracted from Li_3IrO_4 on oxidation without participation of iridium in the redox process. This exacerbated capacity does not come without a cost, since a loss of oxygen and a complete amorphization of the material is observed at the end of charge. This overall oxidation is rationalized by the decomposition enthalpies of Li_xIrO_4 into $Li_xIrO_3 + \frac{1}{2} O_2$ computed for different Li contents (Supplementary Fig. 12) and showing that Li_xIrO_4 starts to be unstable with respect to O_2 release at $x \leq 1$. Interestingly, the resulting a- IrO_3 material has the same stoichiometry and structural IrO_6 connectivity as crystalline β - IrO_3 , obtained from the oxidation of β - Li_2IrO_3 , which is perfectly stable versus oxygen release. Pushing further the calculations, we found that the decomposition of Li_xIrO_4 into $Li_xIrO_3 + \frac{1}{2} O_2$ competes with a structural phase transition that converts the IrO_4 framework, made of condensed chains of edge-shared IrO_6 octahedra, into a more opened framework consisting of fully disconnected IrO_4 tetrahedra (Supplementary Figs. 12 and 13). This Oh to Td transition (Supplementary Table 4) clearly stabilizes the oxygen network, which opens new perspectives to make this transition the winning mechanism over O_2 release. These predictions make the search of stabilizing delithiated Li_xMO_4 structures worth pursuing.

Finally, the possibility to tune the cationic/anionic redox activity of a material by changing the Li/M or O/M ratio represents a great opportunity to prepare new cathode materials as it opens a field previously restricted to layered oxides to the entire family of rocksalt oxides. Furthermore, the vast array of structures existing for the Li_xMO_4 family, exemplified by the $yLi_3RuO_4 - (1-y)Li_3NbO_4$ system¹⁸, opens up a new playground for designing new materials with complex structures. As was observed for the Li_2IrO_3 system⁹, it can also be interesting to search for tridimensional frameworks in order to improve the structural stability on cycling. Thus, an inspiration from this work is rooted in the investigation of ordered rocksalt Li_xMO_4 structures with large capacities and based on well-defined combinations of $3d/4d/5d$ transition metals, a search that could largely benefit from high-throughput theoretical approaches similar to the one recently published on Li_2MO_3 compounds¹⁹.

As a whole, these findings highlight the richness of anionic redox chemistry together with its complexity when designing high-capacity materials, as there is a subtle balance between increasing the number of non-bonding oxygen states and ensuring the stability of the peroxo-like species against oxygen recombination. Fundamentally, the present findings fall in line with our cumulated understanding of the anionic redox activity. Looking forward, by further combining this knowledge with chemical considerations, there is also hope for generating high-capacity and practical Li-based oxides relying on cationic–anionic redox reactions. Designing materials with

increased O/M ratios provides an appealing direction, but a trade-off would have to be found between extra capacity and structural stability, both a blessing and a challenge for further studies.

Methods

Material synthesis and characterization. Li_3IrO_4 was prepared by mixing metallic Ir (Alfa Aesar, 325 mesh, 99.9%) and Li_2CO_3 (Sigma Aldrich, 99%) precursors in stoichiometric proportions using a mortar and pestle. The mix was heated in a covered alumina crucible using a muffle furnace by slowly heating in air at $1^\circ C \text{ min}^{-1}$ up to $950^\circ C$, leaving it at this temperature for 24 h, and finally cooling it naturally to room temperature. Synchrotron X-ray diffraction (XRD) measurements were performed on the 11-BM beamline of the Advanced Photon Source at Argonne National Laboratory, with a wavelength of 0.414 \AA . The neutron diffraction pattern was measured for the reduced material on the D1B powder diffractometer (Institut Laue-Langevin) with a wavelength $\lambda = 1.291 \text{ \AA}$. Diffraction data were refined by the Rietveld method using the hexagonal description of layered $LiMO_2$ phases. The space group, cell parameters and atomic positions are reported in Supplementary Table 1. To prepare the large amount of powder needed for the neutron experiment, a large cell was discharged down to 1.3 V and the electrode recovered after being washed. In situ XRD measurements were performed using an air-tight electrochemical cell equipped with a Be window²⁰ in a BRUKER D8 Advance diffractometer with $Cu K\alpha$ radiation ($\lambda_{K\alpha 1} = 1.54056 \text{ \AA}$, $\lambda_{K\alpha 2} = 1.54439 \text{ \AA}$). The structures of the pristine material and structural transformations on complete charge/discharge were also analysed using transmission electron microscopy (TEM). High-angle annular dark-field scanning TEM images and electron energy-loss spectroscopy data were acquired on a probe aberration-corrected FEI Titan 60-300 microscope. The samples were prepared by dipping holey carbon TEM grids into finely ground powder. A specialized Gatan vacuum transfer holder was used for the analysis.

Electrochemistry. Electrochemical characterization was performed in Swagelok-type cells. The active material was used either as a powder mixed with 20 wt% carbon SP, or as a self-standing electrode prepared by laminating a mixture composed of 5 wt% polytetrafluoroethylene (PTFE), 10 wt% carbon SP and 85 wt% active material. Unless otherwise specified, typical loadings of 10 mg of active materials were used. Metallic lithium was used as the negative electrode and a Whatman GF/D borosilicate glass fibre membrane was used as the separator. The separator was soaked with LP100 electrolyte (1 M $LiPF_6$ in ethylene carbonate (EC)/propylene carbonate (PC)/dimethylcarbonate (DMC) = 1:1:3). The cells were assembled in an Ar-filled glovebox and cycled in galvanostatic mode at rates ranging from C/4 to C/20 (4 to 20 hours/ Li^+).

Gas analysis. In situ measurements of pressure evolution in the cell during galvanostatic cycling were performed using a Swagelok-derived electrochemical cell equipped with a pressure sensor²¹. After assembly, the cell was left to equilibrate at open-circuit voltage for 15 h at a controlled temperature of $25^\circ C$ prior to cycling in order to stabilize the pressure. The cells were then cycled at a rate of C/10 with active material loadings ranging from 5 to 20 mg. Differential electrochemical mass spectrometry (DEMS) measurements were carried out using the same cell, with two additional connections to flush Ar gas in and out to a Hiden Analytical mass spectrometer. The currents of all m/z fragments from 1 to 100 were measured and used to normalize individual contributions. For the DEMS experiment, 1 M $LiPF_6$ in PC was used as an electrolyte and the cell was flushed with Ar for several hours before cycling.

X-ray absorption spectroscopy. Operando X-ray absorption spectroscopy (XAS) measurements at the Ir L_{III} edge were performed in transmission mode at the ROCK beamline²² of synchrotron SOLEIL (France). A Si(111) channel-cut quick-XAS monochromator with an energy resolution of 2 eV at 11 keV was used. The intensity of the monochromatic X-ray beam was measured by three consecutive ionization detectors. The in situ electrochemical cell²⁰ was placed between the first and the second ionization chambers. Self-standing PTFE films of the active material were used and cycled at C/4. One cell was started on reduction to 1.4 V and charged again (cell A). Another was started on oxidation to 4.8 V and discharged (cell B). For the last measurement, an electrode was precharged in a Swagelok cell until $x = 1$ and discharged to $x = 2$, before being transferred to the in situ cell and cycled reversibly between 1.3 and 4 V (cell C). For each cell, successive spectra were collected at a rate of 2 Hz and averaged out over periods of 5 min. The energy calibration was established with simultaneous absorption measurements on an Ir metal foil placed between the second and the third ionization chamber. The data were treated using the Demeter package for energy calibration and normalization²³. The normalized spectra were then globally analysed with principal component analysis²⁴ in order to individuate the orthogonal components able to describe the whole evolution during cycling. The number of principal components was then used as the basis for multivariate curve resolution–alternating least-squares²⁵ analysis. Finally, the reconstructed components were fitted using the Artemis software²³. Fourier transforms of extended X-ray absorption fine-structure (EXAFS) oscillations were carried

out in the k range from 3.5 \AA^{-1} to 16 and 14 \AA^{-1} for crystalline and amorphous components, respectively. Fitting was performed in the R range from 1.0 to 3.6 \AA using the k^3 weight. EXAFS amplitudes and phase shifts were calculated by FEFF7 with a starting model derived from the zigzag chains of Li_3RuO_4 (Supplementary Table 3)²⁶. Except the radial distance (R) and the Debye–Waller factor (σ^2), all other parameters were kept constant (N , E_0 , S_0^2) in the conventional least-squares modelling using the phase and amplitude factors calculated by FEFF7. Error bars for R and σ^2 were estimated from the distribution of values found for the different models tried during the fitting process. The magnitude of the Fourier transform of EXAFS oscillations represents the local atomic distribution around the Ir atom (Supplementary Figs. 8–10). The first peak of Fourier transform corresponds to the nearest six O atoms sitting at $\sim 2 \text{ \AA}$ (peak at $\sim 1.5 \text{ \AA}$), while the second peak is due to the next-nearest two Ir atoms (peak at $\sim 3 \text{ \AA}$). Note that the FTs shown are not corrected for the phase shift. The X-ray absorption near-edge structure (XANES) region close to the white line (WL) was fitted by using an arctangent function for the edge, with fixed width and height, and a single Gaussian function to fit both the t_{2g} and e_g components of the WL. The position and area of the Gaussian were used to follow the changes in energy and intensity of the WL during cycling. The intensity was alternatively calculated by subtracting the arctangent function from the experimental data and integrating the area of the peak, as described in ref. ²⁷, yielding similar results compared to those of the fitting procedure, with the advantage of being independent of the function chosen to fit the WL.

Electron paramagnetic resonance spectroscopy. Ex situ samples for electron paramagnetic resonance (EPR) analysis were recovered in the glovebox after cycling, washed several times with DMC and sealed in a high-purity quartz capillary. EPR samples were collected at 5 K using a Bruker ELEXYS E580 spectrometer operating at 9 GHz . The spectra were recorded with an amplitude modulation of 2 G and microwave power of 5 mW . The spin concentration of samples was calculated with a calibrated weak-pitch sample for organic species and copper sulfate for inorganic ones.

First-principles DFT calculations. Spin-polarized density functional theory (DFT) calculations were performed using the plane-wave density functional theory VASP (Vienna ab initio simulation package) code^{28,29} within the generalized gradient approximation of Perdew–Burke–Ernzerhof (PBE) to describe electron exchange and correlation³⁰. The rotationally invariant Dudarev method (DFT + U)³¹ was used to correct the self-interaction error of conventional DFT for correlated d electrons, through the introduction of an effective on-site Coulomb parameter (U_{eff}) to penalize fractional occupancies in d orbitals³². In the case of the disordered Li_3IrO_4 , the zigzag chain structure of Li_3RuO_4 ²⁶ was employed as a model structure for the calculation and several configurations were computed for delithiated compounds. The crystal structures, electronic properties and electrochemical properties of the Li_xIrO_4 phases were determined for different $U_{\text{eff}} = 0, 2$ and 4 eV .

Data availability. The data that support the plots within this paper and other findings of this study are available from the corresponding author upon reasonable request.

Received: 1 May 2017; Accepted: 29 September 2017;
Published online: 8 December 2017

References

- Koga, H. et al. Reversible oxygen participation to the redox processes revealed for $\text{Li}_{1.20}\text{Mn}_{0.54}\text{Co}_{0.13}\text{Ni}_{0.13}\text{O}_2$. *J. Electrochem. Soc.* **160**, A786–A792 (2013).
- Yabuuchi, N. et al. High-capacity electrode materials for rechargeable lithium batteries: Li_3NbO_4 -based system with cation-disordered rocksalt structure. *Proc. Natl Acad. Sci. USA* **112**, 7650–7655 (2015).
- Freire, M. et al. A new active Li–Mn–O compound for high energy density Li-ion batteries. *Nat. Mater.* **15**, 173–177 (2016).
- Saubanère, M., McCalla, E., Tarascon, J.-M. & Doublet, M.-L. The intriguing question of anionic redox in high-energy density cathodes for Li-ion batteries. *Energy Environ. Sci.* **9**, 984–991 (2016).
- Xie, Y., Saubanère, M. & Doublet, M.-L. Requirements for reversible extra-capacity in Li-rich layered oxides for Li-ion batteries. *Energy Environ. Sci.* **10**, 266–274 (2017).
- Seo, D.-H. et al. The structural and chemical origin of the oxygen redox activity in layered and cation-disordered Li-excess cathode materials. *Nat. Chem.* **8**, 692–697 (2016).
- Sathiya, M. et al. Reversible anionic redox chemistry in high-capacity layered-oxide electrodes. *Nat. Mater.* **12**, 827–835 (2013).
- McCalla, E. et al. Visualization of O–O peroxo-like dimers in high-capacity layered oxides for Li-ion batteries. *Science* **350**, 1516–1521 (2015).
- Pearce, P. E. et al. Evidence for anionic redox activity in a tridimensional-ordered Li-rich positive electrode $\beta\text{-Li}_2\text{IrO}_3$. *Nat. Mater.* **16**, 580–586 (2017).

- Yabuuchi, N., Tahara, Y., Komaba, S., Kitada, S. & Kajiji, Y. Synthesis and electrochemical properties of $\text{Li}_4\text{MoO}_5\text{-NiO}$ binary system as positive electrode materials for rechargeable lithium batteries. *Chem. Mater.* **28**, 416–419 (2016).
- Cabana, J., Monconduit, L., Larcher, D. & Palacin, M. R. beyond intercalation-based Li-ion batteries: the state of the art and challenges of electrode materials reacting through conversion reactions. *Adv. Mater.* **22**, E170–E192 (2010).
- Dahn, J. R., von Sacken, U. & Michal, C. A. Structure and electrochemistry of $\text{Li}_{1-z}\text{NiO}_2$ and a new Li_2NiO_2 phase with the $\text{Ni}(\text{OH})_2$ structure. *Solid State Ion.* **44**, 87–97 (1990).
- Moreau, P., Guyomard, D., Gaubicher, J. & Boucher, F. Structure and stability of sodium intercalated phases in olivine FePO_4 . *Chem. Mater.* **22**, 4126–4128 (2010).
- Qi, B., Perez, I., Ansari, P. H., Lu, F. & Croft, M. L₂ and L₃ measurements of transition-metal 5d orbital occupancy, spin-orbit effects, and chemical bonding. *Phys. Rev. B* **36**, 2972–2975 (1987).
- Choy, J.-H., Kim, D.-K., Demazeau, G. & Jung, D.-Y. LIII-edge XANES study on unusually high valent iridium in a perovskite lattice. *J. Phys. Chem.* **98**, 6258–6262 (1994).
- Choy, J.-H., Kim, D.-K., Hwang, S.-H., Demazeau, G. & Jung, D.-Y. XANES and EXAFS studies on the Ir–O bond covalency in ionic iridium perovskites. *J. Am. Chem. Soc.* **117**, 8557–8566 (1995).
- Zhu, Z. et al. Anion-redox nanolithia cathodes for Li-ion batteries. *Nat. Energy* **1**, 16111 (2016).
- Jacquet, Q. et al. The $\text{Li}_x\text{Ru}_y\text{Nb}_{1-y}\text{O}_4$ ($0 \leq y \leq 1$) system: structural diversity and Li insertion and extraction capabilities. *Chem. Mater.* **29**, 5331–5343 (2017).
- Kim, S. et al. Material design of high-capacity Li-rich layered-oxide electrodes: Li_2MnO_3 and beyond. *Energy Environ. Sci.* **10**, 2201–2211 (2017).
- Leriche, J. B. et al. An electrochemical cell for operando study of lithium batteries using synchrotron radiation. *J. Electrochem. Soc.* **157**, A606–A610 (2010).
- Lepoivre, F., Grimaud, A., Larcher, D. & Tarascon, J.-M. Long-time and reliable gas monitoring in Li–O₂ batteries via a Swagelok derived electrochemical cell. *J. Electrochem. Soc.* **163**, A923–A929 (2016).
- Briois, V. et al. ROCK: the new Quick-EXAFS beamline at SOLEIL. *J. Phys. Conf. Ser.* **712**, 012149 (2016).
- Ravel, B. & Newville, M. ATHENA, ARTEMIS, HEPHAESTUS: data analysis for X-ray absorption spectroscopy using IFEFFIT. *J. Synchrotron Radiat.* **12**, 537–541 (2005).
- Martart, B. et al. *Handbook of Chemometrics and Qualimetrics* (Elsevier, 1997).
- Juan, A., de Jaumot, J. & Tauler, R. Multivariate curve resolution (MCR). Solving the mixture analysis problem. *Anal. Methods* **6**, 4964–4976 (2014).
- Alexander, A. et al. Structural and magnetic properties of Li_3RuO_4 . *J. Mater. Chem.* **13**, 2612–2616 (2003).
- Clancy, J. P. et al. Spin-orbit coupling in iridium-based 5d compounds probed by x-ray absorption spectroscopy. *Phys. Rev. B* **86**, 195131 (2012).
- Kresse, G. & Hafner, J. Ab initio molecular dynamics for liquid metals. *Phys. Rev. B* **47**, 558–561 (1993).
- Kresse, G. & Furthmüller, J. Efficiency of ab-initio total energy calculations for metals and semiconductors using a plane-wave basis set. *Comput. Mater. Sci.* **6**, 15–50 (1996).
- Perdew, J. P., Burke, K. & Ernzerhof, M. Generalized gradient approximation made simple. *Phys. Rev. Lett.* **77**, 3865–3868 (1996).
- Dudarev, S. L., Botton, G. A., Savrasov, S. Y., Humphreys, C. J. & Sutton, A. P. Electron-energy-loss spectra and the structural stability of nickel oxide: An LSDA+ U study. *Phys. Rev. B* **57**, 1505–1509 (1998).
- Anisimov, I., Zaanen, J. & Andersen, O.K. Band theory and Mott insulators: Hubbard U instead of Stoner I . *Phys. Rev. B* **44**, 943–954 (1991).

Acknowledgements

We thank P. Pearce for providing the $\beta\text{-Li}_2\text{IrO}_3$ and L. Lemarquis for helping in the DEMS experiment. We are particularly grateful to S. Belin, V. Briois and L. Stievano for helpful discussions on XAS analysis and synchrotron SOLEIL (France) for providing beamtime at the ROCK beamline (financed by the French National Research Agency (ANR) as part of the ‘Investissements d’Avenir’ programme, reference: ANR-10-EQPX-45). A.J.P. and A.I. acknowledge the GdR C(RS)2 for the workshop organized on a chemometric approach for XAS data analysis. V. Nassif is acknowledged for her help during neutron diffraction experiments performed at Institut Laue Langevin on D1B. Use of the 11-BM mail service of the APS at Argonne National Laboratory was supported by the US Department of Energy under contract No. DE-AC02-06CH11357 and is gratefully acknowledged. This work has been performed with the support of the European Research Council (ERC) (FP/2014)/ERC Grant-Project 670116-ARPEMA.

Author contributions

A.J.P. carried out the synthesis; A.J.P., Q.J., D.L. and J.-M.T. designed and performed the electrochemical studies; A.J.P., Q.J. and G.R. performed the diffraction experiments and

analysis; A.J.P., Q.J. and A.I. carried out the X-ray absorption study; D.B. collected and analysed the TEM images; H.V. collected and analysed the EPR spectra; M.S. and M.-L.D. conducted the DFT study; A.J.P. and J.-M.T. wrote the manuscript and all authors discussed the experiments and edited the manuscript.

Competing interests

The authors declare no competing financial interests.

Additional information

Supplementary information is available for this paper at <https://doi.org/10.1038/s41560-017-0042-7>.

Reprints and permissions information is available at www.nature.com/reprints.

Correspondence and requests for materials should be addressed to J.-M.T.

Publisher's note: Springer Nature remains neutral with regard to jurisdictional claims in published maps and institutional affiliations.